

## Marine mineral-catalyzed NO and N<sub>2</sub>O formation on the anoxic early Earth

S. Buessecker,<sup>1§\*</sup> H. Imanaka,<sup>2,3</sup> T. Ely,<sup>4</sup> R. Hu,<sup>5,6</sup> S.J. Romaniello,<sup>4,7</sup> H. Cadillo-Quiroz<sup>1,8\*</sup>

<sup>1</sup> School of Life Sciences, Arizona State University, Tempe, AZ, USA.

<sup>2</sup> SETI Institute, Mountain View, CA, USA.

<sup>3</sup> NASA Ames Research Center, Moffett Field, CA, USA.

<sup>4</sup> School of Earth and Space Exploration, Arizona State University, Tempe, AZ, USA.

<sup>5</sup> Jet Propulsion Laboratory, California Institute of Technology, Pasadena, CA, USA.

<sup>6</sup> Division of Geological and Planetary Sciences, California Institute of Technology, Pasadena, CA, USA.

<sup>7</sup> Department of Earth and Planetary Sciences, University of Tennessee, Knoxville, TN, USA.

<sup>8</sup> Biodesign Institute, Arizona State University, Tempe, AZ, USA.

§ Current address: Department of Earth System Science, Stanford University, Stanford, CA, USA.

\* Correspondence to: S. Buessecker (sbuessecker@stanford.edu), H. Cadillo-Quiroz (hinsby@asu.edu)

### Abstract

Microbial metabolisms were limited by available terminal electron acceptors in the anoxic environment of the early Archean. However, iron mineral phases in Fe<sup>2+</sup>-rich (ferruginous) oceans could have catalyzed reactions with abiotically fixed nitrogen leading to the formation of nitrous oxide (N<sub>2</sub>O), a potentially favorable terminal electron acceptor. We experimentally simulated anoxic surface-catalyzed reduction of nitrite and nitrate via green rust and magnetite. Besides N<sub>2</sub>O, we detected and quantified the formation of substantial amounts of nitric oxide (NO). While N<sub>2</sub>O escaped into the gas phase (63% of nitrite-nitrogen, with green rust as catalyst), NO remained associated with precipitates (7% of nitrite-nitrogen). Using diffusion and photochemical modeling, we show that marine N<sub>2</sub>O emissions could have sustained atmospheric N<sub>2</sub>O pools of 1-7 ppb. Although this concentration was insufficient to cause significant warming, the seawater enriched in N<sub>2</sub>O and NO could have critically affected early benthic life by providing the opportunity to conserve energy.

## Introduction

The Archean atmosphere prior to the Great Oxidation Event (GOE) was likely dominated by  $N_2$  and  $CO_2$ , with ppm-levels of  $CO$ ,  $CH_4$ , and  $H_2$  (1). The introduction of even trace amounts of more oxidized gases, such as nitrous oxide ( $N_2O$ ), or laughing gas, would have created a significant source of thermodynamic disequilibrium to drive early Archean ecosystems. Microbial  $N_2O$  consumption is based on high-affinity enzymes that are adapted to low  $N_2O$  steady-state concentrations (2). For example, 30 nM  $N_2O$  was readily metabolized in anoxic seawater from modern oxygen minimum zones (3), but the critical  $N_2O$  threshold for marine  $N_2O$  respiration is probably much lower (2).

Despite the proposed key role of  $N_2O$  in the early stages of the Earth's biosphere (4, 5) and climate under a faint young Sun (6), it is unknown whether the ocean acted as a net  $N_2O$  source to the atmosphere prior to  $\sim 2.7$  Ga. While earlier estimates of atmospheric  $N_2O$  abundances were based on biological production rates (7, 8), more recently, abiotic sources of  $N_2O$  have been considered on the early Earth (5, 9). Stanton *et al.* first showed through experiments and modeling that aqueous  $Fe^{2+}$  could have acted as a driver for chemodenitrification to form  $N_2O$  abiotically in Proterozoic oceans (5). Multiple lines of evidence suggest that the oceans were extensively rich in  $Fe^{2+}$  (ferruginous) from  $>3.8$  to  $\sim 2.7$  Ga and had a tendency to export reduced species to the atmosphere (10). The ferrous-ferric hydroxy salt carbonate green rust (GR,  $[Fe^{2+}_{(1-x)}Fe^{3+}_x(OH)_2]^{x+} \cdot [(x/2)CO_3^{2-} \cdot (m/2)H_2O]^x$ ) has been shown to precipitate from Archean seawater-analog solutions, consistent with thermodynamic modeling predicting a predominance of GR in the Fe sink fraction along the water column (11). It has been argued that settling GR particles could have provided a transport mechanism for trace compounds to the seafloor (11), where reducing conditions converted GR to magnetite ( $Fe_3O_4$ ), which is an important constituent of banded iron formations. Nitrogen oxides are prone to become spontaneously reduced in presence of iron mineral phases (12, 13). As a consequence of abiotic nitrogen fixation, nitrite ( $NO_2^-$ ) and nitrate ( $NO_3^-$ ) reached seawater concentrations in the lower  $\mu M$  range (14-17). Geochemical reactions that consume dissolved  $NO_x^-$  species on early Earth include reduction to ammonia (18) and reduction of  $NO_3^-$ ,  $NO_2^-$  and  $N_2$  during water-rock interactions between hydrothermal fluids and the oceanic crust (19, 20). However,  $NO_x^-$  conversion to ammonia is not significant at  $pH \leq 7.3$  (18), a regime that dominated the early oceans (21), and therefore restricted this  $NO_x^-$  sink to more alkaline environments such as ultramafic-hosted hydrothermal vents. In light of the  $NO_x^-$  reduction catalyzing potential of GR and magnetite, the question arises as to whether their precipitation in ferruginous seawater could have driven abiotic reactions that form  $N_2O$  at rates above the photochemical destruction rate. As the major sink for  $N_2O$  is atmospheric photolysis to form  $N_2$ , such reactions could complete a fully abiotic denitrification from  $NO_x^-$  to  $N_2$ , hundreds of millions of years prior to the biological and more efficient production of  $N_2O$  (22).

Here, we evaluated the role of Archean abiotic  $N_2O$  formation, including intermediary NO cycling, from  $NO_x^-$  compounds using microcosm experiments that mimic ferruginous seawater conditions. We used the mixed-valence iron minerals GR and magnetite as catalysts for the reduction of  $NO_2^-$  and  $NO_3^-$  at *low* (1-5  $\mu M$ ), *high* (20-35  $\mu M$ ), and *excessive* (200-350  $\mu M$ ) abundances, and a simple end-member artificial seawater recipe with a 20%  $CO_2$ - $HCO_3^-$  buffer devoid of sulfur. These experiments, together with diffusive and photochemical models, allowed us to estimate NO and  $N_2O$  abundances in the ocean-atmosphere system of the Archean.

## Results and Discussion

***Iron mineral reactions with nitrate and nitrite under simulated Archean ocean conditions.*** We first compared the reactivity of  $\text{NO}_2^-$  and  $\text{NO}_3^-$  with GR, magnetite and aqueous  $\text{Fe}^{2+}$  separately. For all reductants, consumption of  $\text{NO}_3^-$  and  $\text{N}_2\text{O}$  production was negligible ( $< 0.03 \text{ nmol h}^{-1}$ , Fig. 1A) even over a prolonged period of 100 days. In contrast,  $\text{NO}_2^-$  showed reactivity in the presence of both mineral catalysts, and was stable in controls with  $500 \text{ }\mu\text{M}$  aqueous  $\text{Fe}^{2+}$ . The contrasting reactivity of the nitrogen oxides was also reflected in the solid phase  $\text{Fe}^{2+}/\text{Fe}^{3+}$  ratio determined at the end of the experiment (Fig. 2), revealing a trend of higher mineral oxidation with increasing  $\text{NO}_2^-$  concentration. Magnetite and GR showed disparate potential to produce  $\text{N}_2\text{O}$ . Concomitant with a more rapid  $\text{NO}_2^-$  consumption,  $\text{N}_2\text{O}$  production rates were more than 10 times higher when GR was the catalyst (Fig. 1B). At GR surface areas as observed for the Archean ocean analogue Lake Matano, Indonesia ( $\sim 10^{-3} \text{ m}^2 \text{ mL}^{-1}$ , 23, Fig. 1C), abiotic  $\text{N}_2\text{O}$  production rates were 25% (*low*  $\text{NO}_2^-$ ) and  $>200\%$  (*high*  $\text{NO}_2^-$ ) the biotic production rates measured in modern oxygen minimum zones ( $\sim 1 \text{ nM day}^{-1}$ , 24). As a reference, modern  $\text{NO}_2^-$  concentrations are near the bottom of the experimental range employed here, which extends higher to account for a range of possible Archean  $\text{NO}_x$  abundances (see below).

The conversion of  $\text{NO}_2^-$  to  $\text{N}_2\text{O}$  was not equimolarly balanced and we therefore considered accumulation of NO as intermediary species (25). After observing an initial modest NO accumulation, we injected concentrated hydrochloric acid in order to dissolve mineral particles and release any fraction bound to mineral surfaces (Fig. 1D). Indeed, the dissolution of mineral particles was followed by a spike in headspace NO concentration. At least 92% of the total amount of NO produced was bound to GR surfaces (97% was bound to magnetite surfaces). To rule out reaction of the acid itself with residual  $\text{NO}_2^-$ , we conducted controls with sulfuric acid and  $\text{NO}_2^-$  (table S2). Other controls to evaluate the stability of NO in the mineral suspension included acid injection at later time points in time-extended experiments observing NO yields at 220 hours ( $< 2.5 \text{ }\mu\text{M NO}_2^-$ ) similar to those at 50 hours after  $\text{NO}_2^-$  addition (table S2). We calculated the yield of NO in respect to the total added  $\text{NO}_2^-$  and, accordingly, 7% reacted to NO (over 63% that reacted to  $\text{N}_2\text{O}$ ) with GR as catalyst and 69% reacted to NO (over 8% that reacted to  $\text{N}_2\text{O}$ ) with magnetite as catalyst. The remaining product pool could be  $\text{N}_2$  (25) and would only constitute a minor fraction of the total added nitrogen. Our data show that mineral-associated NO, presumably in the form of nitrosyl species (26), is a significant byproduct and geochemically stable in presence of Fe mineral phases.

***Marine emissions accumulate atmospheric  $\text{N}_2\text{O}$ .*** To elucidate the impact of the experimentally derived production rates for the dispersion of  $\text{N}_2\text{O}$  in the seawater and emission to the Archean atmosphere, we combined diffusion models into a simple flux balance model (supplementary materials). We considered a 100 m deep slab of ocean beneath the photic zone as the part of the water column with a maximum overlap of  $\text{NO}_x^-$  ions from the surface and GR formation fueled by upwelling water rich in  $\text{Fe}^{2+}$  from the depth. An estimate of the GR particle concentration in the Archean ocean was informed by observed Fe particle numbers from seven modern marine and freshwater anoxic basins (supplementary materials), including the anoxic lake basin Kabuno Bay (KB) in East Africa (27). The peak  $\text{Fe}^{2+}$  concentration in the particulate fraction of KB anoxic waters ( $11 \text{ }\mu\text{M}$ ) closely reflects concentrations used for the thermodynamic modeling of GR precipitation in Archean seawater (11), which is why we used KB levels as a reference and enveloped that value with a putative lower and upper boundary of 50% and 500%. Archean seawater  $\text{Fe}^{2+}$  could have reached concentrations of  $55 \text{ }\mu\text{M}$ , as constrained by  $\text{Fe}^{2+}$

toxicities on cyanobacteria (28) and the appearance of herringbone and micritic carbonates (29, 30). At that upper boundary and under *low*  $\text{NO}_2^-$  conditions, net  $\text{N}_2\text{O}$  emissions conceivably reached 235 [98.1–413.9]  $\text{nmol m}^{-2} \text{h}^{-1}$  (95% CI, fig. S7, table S4), implicating 4 times the modern marine average flux (31). Overall,  $\text{N}_2\text{O}$  emissions from the ferruginous ocean gradually increased with the GR particle concentration in the water column.

To simulate the effect of  $\text{N}_2\text{O}$  fluxes triggered by mineral catalysis into an anoxic Archean atmosphere, we applied a photochemical model (32). We probed four different  $\text{N}_2\text{O}$  fluxes corresponding to *low* and *high*  $\text{NO}_2^-$  levels and  $\text{Fe}^{2+}$  concentrations in GR phases around the KB reference (table S4). Although the upper boundary of our estimates implicated near-modern  $\text{N}_2\text{O}$  abundances in the troposphere (0-13 km altitude, Fig. 3),  $\text{N}_2\text{O}$  concentration boundaries derived from *low*  $\text{NO}_2^-$  seawater levels and predicted to be 1-7 ppb are more realistic. This lower range is analogous to mixing ratios from Proterozoic atmosphere models assuming 1% of present oxygen levels (5, 8). A striking difference is, however, the source of  $\text{NO}_x^-$  compounds, which was assumed to be microbial nitrification in the Proterozoic and abiotic nitrogen fixation prior to the GOE. Thus, abiotically derived  $\text{NO}_x^-$  can potentially produce tropospheric  $\text{N}_2\text{O}$  levels equal to those from biological origins.

Because of prevailing ferruginous conditions, the mineral reactions were likely limited by abiotic nitrogen fixation rates rather than mineral surface area. Previous seawater  $\text{NO}_x^-$  estimations – 8.7-24,000  $\mu\text{M}$  (16), 1-10,000  $\mu\text{M}$  (20), <1  $\mu\text{M}$  (17) and 0.2-2  $\mu\text{M}$  (33) – reveal a large uncertainty. For comparison, modern  $\text{NO}_2^-$  concentrations reach ~1.5  $\mu\text{M}$  around oxygen minimum zones, but contrary to the Archean ocean, oxidoreductases effectively suppress  $\text{NO}_2^-$  accumulation (34). The associated nitrogen fixation rates differ between these studies. We carefully chose the initial  $\text{NO}_x^-$  concentrations in order to cover the lower end of the estimates, but also to demonstrate feasible reactions over at least two orders of magnitude in possible concentrations. Ongoing mineral reactions could further draw down  $\text{NO}_x^-$  concentrations, especially in proximity to particles, if consumption exceeded diffusion of new reactant. During active consumption,  $\text{NO}_x^-$  ions would diffuse from surface (0-40 m) and deeper (>140 m) water layers to mineral precipitates and replenish reactant. If mineral reactions indeed lowered local seawater  $\text{NO}_x^-$  concentrations, atmospheric  $\text{N}_2\text{O}$  may have reached sub-ppb concentrations, but not lower than HNO<sub>3</sub>-derived  $\text{N}_2\text{O}$  concentrations (>0.5 ppb, Fig. 3). While the estimates from previous studies refer to the bulk seawater composition (values are average concentrations), top-down gradients of  $\text{NO}_x^-$  or conical zones of higher  $\text{NO}_x^-$  concentrations beneath rain out areas (Fig. 4) contributed perhaps to a more heterogeneous distribution. In such zones,  $\text{NO}_x^-$  may have reached concentrations well above the *low*  $\text{NO}_x^-$  range (1-5  $\mu\text{M}$ ) designated here, thus, justifying the inclusion of  $\text{N}_2\text{O}$  fluxes based on higher  $\text{NO}_x^-$  abundances.

The main sink of  $\text{N}_2\text{O}$  is photolysis by radiation < 230 nm (35) in the stratosphere, which governs the shape of the concentration profiles (Fig. 3). In the Archean atmosphere,  $\text{N}_2\text{O}$  abundances could have been higher due to i) additional sources and ii) protective agents against UV light. For instance, high-energy particles from solar flares led to  $\text{N}_2\text{O}$  formation most active at higher altitudes and could complement surface sources (9). These pathways played perhaps a more significant role in the Hadean or early Archean when the Sun was more active and the magnetic field openings were greater at the poles.

Furthermore, in the presence of methane hazes as proposed for the Archean,  $\text{N}_2\text{O}$  could have been shielded through strong UV absorption by fractal haze particles (36), which prolonged its lifetime. Both processes could have helped to stabilize atmospheric  $\text{N}_2\text{O}$  abundances that resulted from mineral-catalyzed  $\text{N}_2\text{O}$  production in the oceans.

Despite the tropospheric abundances predicted by our model, effects on the planetary climate were probably modest because  $\text{N}_2\text{O}$  would not be sufficiently concentrated to significantly increase the infrared atmospheric opacity in the  $\text{CO}_2$  window regions. Especially in high  $\text{CO}_2$  atmospheres, the  $\text{N}_2\text{O}$  radiative forcing is diminished since it may not occupy otherwise transparent infrared windows. The infrared window between 6 and 8  $\mu\text{m}$  could potentially be filled by  $\text{N}_2\text{O}$  absorption, but this is dependent on atmospheric methane which absorbs at similar wavelengths (8). Since methane concentrations were likely  $> 100$  ppmv (37), greenhouse warming by  $\text{N}_2\text{O}$  under our simulated conditions therefore contributed only weakly to a warmer climate under the faint young Sun of the Archean (6).

***Effects of NO and  $\text{N}_2\text{O}$  on early anaerobic microbial life.*** It is plausible that as life co-evolved with the Earth system (38), it could have done so on a molecular level as an adaptation to abiotic NO and  $\text{N}_2\text{O}$  fluxes, too. Given GR phases at 100% KB equivalence, low seawater  $\text{NO}_2^-$  levels, and a 70% ocean cover of Earth's surface,  $\text{N}_2\text{O}$  emissions exported  $10.4 \text{ Tg N yr}^{-1}$  into the Archean atmosphere. Because of its high solubility, the fraction of  $\text{N}_2\text{O}$  dissolved in the ocean should not be underestimated. Under generally accepted Archean ocean conditions,  $\text{N}_2\text{O}$  reduction to  $\text{N}_2$  is thermodynamically favorable. For example, coupled to  $\text{H}_2$  oxidation ( $\text{H}_2$  as a simple and available reductant), an affinity of up to 300 kcal per electron accepted by  $\text{N}_2\text{O}$  is significantly higher than that of any other redox reaction tested (fig. S8). Significant amounts of mineral surface-bound NO could have been transported down to the seafloor by settling of GR precipitates. Assuming a particle sinking velocity of  $50 \text{ m day}^{-1}$  (39),  $1.2 \text{ Tg N yr}^{-1}$  in the form of NO could have reached ocean sediments. This constitutes only  $\sim 1\%$  of the downward  $\text{NO}_3^-$  flux (as comparable nitrogen oxide) measured above today's continental shelves (40). However, GR-shuttling of NO molecules may have been effective to reach benthic microbial life, where it then acted as a biological electron sink (41, Fig. 4). The availability of NO may have been essential for early denitrifying microorganisms because marine sediments in the Archean lacked nitrification as a source of nitrogen oxides. Conversely, NO could have also been damaging to microorganisms. The inhibitory effects of the NO molecule are well known and include production of radicals and the stimulation of nitrosative stress (42). In either case, NO exerted selective pressure and shaped the community composition. Based on enzymatic structural resemblance of NO and  $\text{N}_2\text{O}$  reductases (Nor and Nos) with cytochrome c oxidase (5, 43, 44) a primitive form of  $\text{N}_2\text{O}$  reduction likely preceded aerobic respiration. This concept is supported by a simple make-up of the respiratory chains involving quinone-dependent Nor and membrane-bound Nos, as present in some gram(+) bacteria (4, 45). Evidently, the existence of NO and  $\text{N}_2\text{O}$  in the water column could have been feasibly exploited for the conversion of free energy and can at least explain biochemical patterns in modern respiratory enzyme complexes.

## Conclusion

Our findings show that a significant portion of  $\text{NO}_x^-$  in the ferruginous Archean ocean was likely diverted to  $\text{N}_2\text{O}$  and  $\text{NO}$  leading to more oxidized products when compared to other sink pathways (ending in  $\text{N}_2$  or ammonia). If this was the case, then the degree of thermodynamic disequilibria in the redox balance of the Archean nitrogen cycle may have been underestimated (46). Correspondingly, we caution to use  $\text{N}_2\text{O}$  as unique biosignature in exoplanet exploration. It is possible that conditions for the mineral-catalyzed  $\text{N}_2\text{O}$  production on early Earth-like exoplanets are even more favorable, resulting in  $\text{N}_2\text{O}$  atmospheric concentrations that could exceed modern ones (higher abiotic nitrogen fixation rates, higher Fe mineral load). Signals could be interpreted as false positives without any biological basis.

We present evidence that higher ozone levels may not be required to reach ppb  $\text{N}_2\text{O}$  concentrations prior to the GOE and lay out a concept of a complete abiotic  $\text{N}_2\text{O}$  cycle driven by mineral-catalyzed reactions (Fig. 4). Rather than being a mainly biological invention, the reduced branch of the abiotic nitrogen cycle was seemingly co-opted by early organisms. Even though the effects of abiotic  $\text{N}_2\text{O}$  production were probably modest on the early climate, marine sources of  $\text{N}_2\text{O}$  and  $\text{NO}$  could have markedly influenced the evolution of microbial respiration.

## Materials and Methods

*Mineral synthesis.* Carbonate green rust was synthesized according to the following. In brief, 18.2 MΩ·cm water was made anoxic by boiling and sparging with  $\text{CO}_2/\text{N}_2$  (20:80). An anoxic 0.4 M  $\text{Fe}^{2+}/\text{Fe}^{3+}$  solution (0.1 L) was prepared by mixing 7.42 g of  $\text{FeSO}_4 \cdot 7 \text{H}_2\text{O}$  (>99%, Sigma Aldrich) and 2.66 g of anhydrous  $\text{Fe}_2(\text{SO}_4)_3$  (97%, Sigma Aldrich). An alkaline, anoxic solution of 0.466 M  $\text{Na}_2\text{CO}_3$  (Fisher Scientific) in 0.8 M  $\text{NaOH}$  (Fisher Scientific) (0.1 L) was prepared by dissolving  $\text{NaOH}$  first under a constant stream of  $\text{CO}_2/\text{N}_2$  gas, after which  $\text{Na}_2\text{CO}_3$  was added. Both solutions were stirred continuously at 500 rpm. The alkaline solution was injected into the  $\text{Fe}^{2+}/\text{Fe}^{3+}$  solution using  $\text{CO}_2/\text{N}_2$  flushed syringes. Precipitation occurred immediately and the suspension was stirred in the dark for 24 hours. Magnetite was synthesized as nanoparticles following previously described protocols (47, 48).

*Mineral harvest.* Green rust and magnetite precipitates were washed in an anaerobic chamber (0.5%  $\text{H}_2$  in  $\text{N}_2$ , Coy Laboratory Products) using a vacuum filtration unit (Nalgene, Mfr # 130-4020) and 0.45 μm cellulose-acetate filter membranes (Sartorius). Anoxic 18.2 MΩ·cm water was poured onto the precipitates for a minimum of 8 cycles (pouring followed by extracting water). When filtrate flow ceased to a minimum, the wet mineral paste was removed from the filter. Wet carbonate green rust (73.8% water content) and wet magnetite (47.2% water content) were added to microcosms. The wet minerals were also used for mineralogical characterization (XRD and microscopy). For BET analysis, a defined amount of precipitate was dried in small boxes filled with drierite and placed into the anaerobic chamber. Dry weight was constant after 3-5 days.

*X-ray diffractometry (XRD).* Powder X-ray diffractometry was conducted on a subset of samples after synthesis and washing of the mineral products. A glycerol smear was prepared with 10 mg sample in the anaerobic chamber and sealed in a glass vial to prevent oxidation prior to analysis. To collect the XRD data, the sample was removed from the vial and spread across a quartz zero background plate that was placed onto a horizontal stage in a Bruker D-5000 diffractometer (Bruker, Germany) equipped with a Co K $\alpha$  X-ray tube (30 kV,  $\lambda = 1.791 \text{ \AA}$ ). Signal peaks were compared to reference diffractograms in the RRUFF database. Instrument broadening was determined by a standard polycrystalline alumina sample. X-ray diffractometry data was analyzed with the CrystalDiffract software version 6.8.2 for Mac.

*Scanning- and transmission-electron microscopy (SEM, TEM).* Samples for SEM imaging were mounted on aluminum pin stubs with double-sided carbon tabs in the glove box and transported in a sealed jar with anoxic atmosphere to the microscope. Samples were not sputter-coated. Images were taken on an XL30 ESEM-FEG (Philips) operated at a 30 kV accelerating voltage and a 21 pA beam current. TEM samples were dispersed on a Lacey Carbon film using 200 mesh copper grids. The instrument used was a CM200 Field Emission Microscope at 200KV (Philips) with  $C_s = 1.2 \text{ mm}$  and a PTP resolution of 0.25 nm. Imaging was done on a Gatan Orius CCD system.

*Brunauer-Emmett-Teller (BET) surface area measurements.* For analysis of the BET surface area, dried mineral precipitate was weighed inside the anaerobic chamber and added to a Florence glass flask that was closed with a rubber stoppers for transport to the instrument. BET surface in replicate samples ( $n = 3$  for GR,  $n = 2$  for magnetite) was quantified using  $N_2$  gas on a Tristar II 3020 analyzer (Micromeritics Inc.). The instrument has a limit of detection of  $1 \text{ m}^2$ . Our results (table S1) are roughly consistent with previously determined BET values of  $47 \text{ m}^2 \text{ g}^{-1}$  for GR (49) and  $95 \text{ m}^2 \text{ g}^{-1}$  for magnetite (50).

We performed calculations of the mineral surface area for both minerals to supplement our measurements. To derive the mineral density, we calculated the average crystallite size by inserting the full width at half maximum, as determined from the diffractograms and the Bragg angle of the GR 0 0 3 reflection and of the magnetite 3 1 1 reflection, into the Scherrer equation. Mineral density was calculated using the formula  $\rho = (M \cdot Z) / (V_c \cdot 0.60225)$  where  $M$  is molar mass,  $Z$  is the number of molecules per crystallite and  $V_c$  is crystallite size. The density and the grain volume as measured by TEM/SEM were used to calculate the grain mass. The final value in  $\text{m}^2 \text{ g}^{-1}$  was derived from the grain mass and the grain surface area (TEM/SEM). For magnetite, we calculated a surface area of  $88.8 \text{ m}^2 \text{ g}^{-1}$ . For green rust, we calculated a minimum approximation (surface of green rust sheets only) of  $27.6 \text{ m}^2 \text{ g}^{-1}$  and a maximum approximation (including surface between sheets) of  $538.5 \text{ m}^2 \text{ g}^{-1}$ . Thus, our measured value for magnetite is somewhat lower than the calculated and literature value. The measured value for green rust is in good agreement with the literature value and at the lower end of the calculated range.

*Incubation conditions.* Interactions of nitrogen oxides with Fe minerals were tested in anoxic microcosms designed to mimic Archean ocean conditions as closely as possible. Borosilicate glass bottles (30-120 mL) were closed with thick butyl rubber stoppers and a headspace of 20%  $CO_2$  in  $N_2$  was used throughout the experiment. All

glassware was washed with 2 M HCl prior to use. The liquid phase constituted one third of the microcosm total volume. We used a published recipe for artificial Archean seawater (51) and omitted any sulfur species. The pH was initially set to 7.3 using a  $\text{CO}_2\text{--HCO}_3^-$  buffer. We boiled 18.2 M $\Omega$ ·cm water and sparged it with  $\text{CO}_2/\text{N}_2$  (20:80) while it was cooling on ice. Salts were added during the sparging. The anoxic solution was then dispensed with a pipetor into microcosms in an anaerobic chamber (0.5%  $\text{H}_2$  in  $\text{N}_2$ , Coy Laboratory Products). Nitrate and nitrite stock solutions were prepared with their respective sodium salts  $\text{NaNO}_3$  ( $\geq 99\%$ , Fisher Scientific) and  $\text{NaNO}_2$  ( $\geq 97\%$ , Acros Organics) and dissolved in artificial seawater. The solutions were then sparged with  $\text{N}_2$  and filter-sterilized (0.8/0.2  $\mu\text{m}$  pore size, VWR) in the anaerobic chamber. Controls with aqueous  $\text{Fe}^{2+}$  were prepared in anoxic artificial seawater and  $\text{FeCl}_2$  ( $\geq 99\%$ , Fisher Scientific). Wet minerals were weighed in the anaerobic chamber and distributed into microcosms using ethanol-washed plastic spatulas. Prior to start of the incubations with the injection of the  $\text{NO}_x^-$  solution, mineral agglomerates were dissipated in an ultrasonic bath (Ultrasonic cleaner 2510, Branson Ultrasonics). Microcosms were shaken at 250 rpm in the dark and at room temperature over the whole duration of the experiment. Controls were incubated in the anaerobic chamber to test for potential leaking through stoppers, which did not occur. To dissolve mineral particles during incubations, 1.6 mL of concentrated 12N HCl or 37N  $\text{H}_2\text{SO}_4$  was slowly injected through bottle septa to 10 mL mineral seawater-suspension. Dissolution of solid particles occurred instantly and the liquid first turned turbid orange-green and then clear green-yellow (HCl) or light yellow ( $\text{H}_2\text{SO}_4$ ) within 15-20 hours. The last measurement of NO in the headspace was taken when the liquid was clear (fig. S5).

*Dissolved nitrite, nitrate, ammonium, ferrous and ferric iron measurements.* All dissolved analytes were quantified spectrometrically with plate assays. Nitrite in solution was quantified with the Griess reagent (Promega, Kit G2930). Nitrate was first reduced to nitrite by vanadium(III) chloride and then quantified as nitrite (52). Ammonium production was verified with the salicylic acid assay (53). To determine the  $\text{Fe}^{2+}/\text{Fe}^{3+}$  solid phase ratio, mineral particles were settled, after which supernatant artificial seawater was removed from the microcosms. Anoxic acidic extraction of green rust and magnetite was conducted as described previously (47). Ferrous and ferric ions in the extracts were measured by reaction with ferrozine after the method of Stookey (54).

*$\text{N}_2\text{O}$  gas measurements.* To quantify  $\text{N}_2\text{O}$  production, 200  $\mu\text{L}$  of headspace gas was sampled with a gas-tight syringe (VICI Precision Sampling) and injected onto a gas chromatograph (GC, SRI Instruments) equipped with an electron-capture detector (ECD). Two continuous HayeSep-D columns were kept at 90°C (oven temperature) and  $\text{N}_2$  (UHP grade 99.999%, Praxair Inc.) was used as carrier gas. The ECD current was 250 mV and the ECD cell was kept at 350°C. The  $\text{N}_2\text{O}$  measurements were calibrated using customized standard mixtures (Scott Specialty Gases, accuracy  $\pm 5\%$ ) over a range of 0.25–100 ppmv. Gas accumulation in the microcosms was monitored over time. Gas concentrations were corrected using Henry's law and the dimensionless concentration constant  $k_H^{cc}(\text{N}_2\text{O}) = 0.6112$  to account for gas partitioning into the aqueous phase at 25°C.

*NO gas measurements.* Nitric oxide (NO) was quantified in the microcosm headspace with a chemiluminescence-based analyzer (LMA-3D  $\text{NO}_2$  analyzer, Unisearch Associates Inc.). Headspace gas (50  $\mu\text{L}$ ) was withdrawn with a  $\text{CO}_2\text{--N}_2$ -flushed gas-tight syringe and injected into the analyzer. The injection port was customized to fit the injection



volume and consisted of a T-junction with an air filter at one and a septum at the other end. An internal pump generated consistent airflow. In short, sample NO was oxidized to NO<sub>2</sub> by a CrO<sub>3</sub> catalyst. The NO<sub>2</sub> flew across a fabric wick saturated with a Luminol solution. Luminol was obtained from Drummond Technology Inc. (Canada). Readings were corrected for background NO<sub>2</sub> every 15 minutes (“zeroing”). Shell airflow rate was kept at 500 mL min<sup>-1</sup> and the span potentiometer was set to 8. Measurements were calibrated with a 0.1 ppm NO (in N<sub>2</sub>) standard (<0.0005 ppm NO<sub>2</sub>, Scott-Marine Inc.) over a range of 5–1,000 ppbv. Gas concentrations were corrected using Henry’s law and the dimensionless concentration constant  $k_H^{cc}(\text{NO}) = 0.0465$  to account for gas partitioning into the aqueous phase at 25°C.

*Diffusion modeling.* The partial fluxes of the overall flux balance  $\Phi_{\text{sed}} + \Phi_{\text{par}} = \Phi_{\text{atm}}$  were normalized to a 100 m vertical slab with 1 m<sup>2</sup> basis. The upper 100 m ocean water are typically considered as well-mixed, hence, reactant and catalyst are homogeneously distributed in that space. Depending on the water depth, a portion of the NO<sub>x</sub> could reach the ocean floor, which is why we added a generic sediment flux ( $\Phi_{\text{sed}}$ ) to the balance equation. The dominant flux would emerge from floating GR mineral particles ( $\Phi_{\text{par}}$ ) that are distributed along the water column. For simplicity, we assume that all GR had aged into magnetite in the sediment and all floating particles were GR phases. We refer to the supplementary material for a more detailed description of the derivation of the partial fluxes, the error propagation method, and thermodynamic calculations.

*Photochemical modeling.* We have used an atmospheric photochemistry model to simulate the effects of N<sub>2</sub>O emission into an anoxic atmosphere akin to the Archean Earth’s condition. The photochemistry model used (32, 55) has been validated by computing the atmospheric compositions of present-day Earth and Mars, as the outputs agreed with the observations of major trace gases in Earth’s and Mars’ atmospheres (56). For this work, we simulate a 1-bar atmosphere of 95% N<sub>2</sub> and 5% CO<sub>2</sub> to approximate the anoxic and CO<sub>2</sub>-rich environment of the Archean Earth. We assume a surface temperature of 288 K and a stratospheric temperature of 200 K, and adopt the eddy diffusion coefficient derived from the number density profiles of trace gases on Earth (57). The photochemistry model includes a comprehensive reaction network for O, H, C, N, and S species including sulfur and sulfuric acid aerosols, and includes volcanic outgassing of CO, H<sub>2</sub>, SO<sub>2</sub>, and H<sub>2</sub>S. The outgassing rate is not high enough to produce a H<sub>2</sub>SO<sub>4</sub> aerosol layer in the atmosphere.

## References and Notes

1. J. F. Kasting, Atmospheric composition of Hadean – early Archean Earth: The importance of CO. *Geological Society of America Special Papers*, 19–28 (2014).
2. S. Yoon *et al.*, Nitrous oxide reduction kinetics distinguish bacteria harboring clade I nosz from those harboring clade II NosZ. *Appl. Environ. Microbiol.* **82**, 3793–3800 (2016).
3. A. R. Babbin, D. Bianchi, A. Jayakumar, B. B. Ward, Rapid nitrous oxide cycling in the suboxic ocean. *Science*. **348**, 1127–1129 (2015).

- 438 4. J. Chen, M. Strous, Denitrification and aerobic respiration, hybrid electron transport  
439 chains and co-evolution. *Biochimica et Biophysica Acta (BBA) - Bioenergetics*. **1827**,  
440 136–144 (2013).
- 441 5. C. L. Stanton *et al.*, Nitrous oxide from chemodenitrification: A possible missing link in  
442 the Proterozoic greenhouse and the evolution of aerobic respiration. *Geobiology*. **16**,  
443 597–609 (2018).
- 444 6. D. O. Gough, in *Physics of Solar Variations* (Springer, Dordrecht, 1981), pp. 21–34.
- 445 7. L. V. Godfrey, P. G. Falkowski, The cycling and redox state of nitrogen in the Archaean  
446 ocean. *Nature Geoscience*. **2**, 725–729 (2009).
- 447 8. A. L. Roberson, J. Roadt, I. Halevy, J. F. Kasting, Greenhouse warming by nitrous oxide  
448 and methane in the Proterozoic Eon. *Geobiology*. **9**, 313–320 (2011).
- 449 9. V. S. Airapetian, A. Gloer, G. Gronoff, E. Hébrard, W. Danchi, Prebiotic chemistry  
450 and atmospheric warming of early Earth by an active young Sun. *Nature Geoscience*. **9**,  
451 452–455 (2016).
- 452 10. S. W. Poulton, D. E. Canfield, Ferruginous conditions: A dominant feature of the ocean  
453 through Earth's history. *Elements*. **7**, 107–112 (2011).
- 454 11. I. Halevy, M. Alesker, E. M. Schuster, R. Popovitz-Biro, Y. Feldman, A key role for  
455 green rust in the Precambrian oceans and the genesis of iron formations. *Nature*  
456 *Geoscience*. **10**, 135–139 (2017).
- 457 12. J. Sorensen, L. Thorling, Stimulation by lepidocrocite ( $\gamma$ -FeOOH) of Fe(II)-dependent  
458 nitrite reduction. *Geochimica et Cosmochimica Acta*. **55**, 1289–1294 (1991).
- 459 13. H. Hansen, O. K. Borggaard, J. Sorensen, Evaluation of the free energy of formation of  
460 Fe(II)-Fe(III) hydroxide-sulphate (green rust) and its reduction of nitrite. *Geochimica et*  
461 *Cosmochimica Acta*. **58**, 2599–2608 (1994).
- 462 14. R. L. Mancinelli, C. P. McKay, The evolution of nitrogen cycling. *Orig Life Evol*  
463 *Biosph*. **18**, 311–325 (1988).
- 464 15. D. P. Summers, B. Khare, Nitrogen fixation on early Mars and other terrestrial planets:  
465 experimental demonstration of abiotic fixation reactions to nitrite and nitrate.  
466 *Astrobiology*. **7**, 333–341 (2007).
- 467 16. M. L. Wong, B. D. Charnay, P. Gao, Y. L. Yung, M. J. Russell, Nitrogen oxides in early  
468 Earth's atmosphere as electron acceptors for life's emergence. *Astrobiology*. **17**, 975–  
469 983 (2017).
- 470 17. S. Ranjan, Z. R. Todd, P. B. Rimmer, D. D. Sasselov, A. R. Babbitt, Nitrogen oxide  
471 concentrations in natural waters on early Earth. *Geochemistry, Geophysics, Geosystems*.  
472 **20**, 2021–2039 (2019).
- 473 18. D. P. Summers, S. Chang, Prebiotic ammonia from reduction of nitrite by iron (II) on  
474 the early Earth. *Nature*. **365**, 630–633 (1993).

- 475 19. J. A. Brandes *et al.*, Abiotic nitrogen reduction on the early Earth. *Nature*. **395**, 365–367  
476 (1998).
- 477 20. M. Laneuville, M. Kameya, H. J. Cleaves II, Earth without life: A systems model of a  
478 global abiotic nitrogen cycle. *Astrobiology*. **18**, 897–914 (2018).
- 479 21. I. Halevy, A. Bachan, The geologic history of seawater pH. *Science*. **355**, 1069–1071  
480 (2017).
- 481 22. R. Buick, Did the Proterozoic “Canfield Ocean” cause a laughing gas greenhouse?  
482 *Geobiology*. **5**, 97–100 (2007).
- 483 23. A. Zegeye *et al.*, Green rust formation controls nutrient availability in a ferruginous  
484 water column. *Geology*. **40**, 599–602 (2012).
- 485 24. Q. Ji, A. R. Babbin, A. Jayakumar, S. Oleynik, B. B. Ward, Nitrous oxide production by  
486 nitrification and denitrification in the Eastern Tropical South Pacific oxygen minimum  
487 zone. *Geophysical Research Letters*. **42**, 10,755–10,764 (2015).
- 488 25. K. C. Grabb, C. Buchwald, C. M. Hansel, S. D. Wankel, A dual nitrite isotopic  
489 investigation of chemodenitrification by mineral-associated Fe(II) and its production of  
490 nitrous oxide. *Geochimica et Cosmochimica Acta*. **196**, 388–402 (2017).
- 491 26. A. D. Gordon *et al.*, Reduction of nitrite and nitrate on nano-dimensioned FeS. *Orig Life  
492 Evol Biosph.* **43**, 305–322 (2013).
- 493 27. M. Llíros *et al.*, Pelagic photoferrotrophy and iron cycling in a modern ferruginous  
494 basin. *Scientific Reports* 2015 5. **5**, 1–8 (2015).
- 495 28. E. D. Swanner *et al.*, Modulation of oxygen production in Archean oceans by episodes  
496 of Fe(II) toxicity. *Nature Geoscience*. **8**, 126–130 (2015).
- 497 29. D. Y. Sumner, Carbonate precipitation and oxygen stratification in late Archean  
498 seawater as deduced from facies and stratigraphy of the Gamohaan and Frisco  
499 formations, Transvaal Supergroup, South Africa. *American Journal of Science*. **297**,  
500 455–487 (1997).
- 501 30. D. Y. Sumner, J. P. Grotzinger, Were kinetics of Archean calcium carbonate  
502 precipitation related to oxygen concentration? *Geology*. **24**, 119 (1996).
- 503 31. G. Battaglia, F. Joos, Marine N<sub>2</sub>O emissions from nitrification and denitrification  
504 constrained by modern observations and projected in multimillennial global warming  
505 simulations. *Global Biogeochemical Cycles*. **32**, 92–121 (2018).
- 506 32. R. Hu, S. Seager, W. Bains, Photochemistry in terrestrial exoplanet atmospheres. I.  
507 Photochemistry model and benchmark cases. *ApJ*. **761**, 1–29 (2012).
- 508 33. R. Hu, H. D. Diaz, Stability of nitrogen in planetary atmospheres in contact with liquid  
509 water. *ApJ*. **886**, 1–8 (2019).
- 510 34. M. A. Saito *et al.*, Abundant nitrite-oxidizing metalloenzymes in the mesopelagic zone  
511 of the tropical Pacific Ocean. *Nature Geoscience*. **13**, 355–362 (2020).

- 512 35. J. Kaiser, T. Röckmann, C. A. M. Brenninkmeijer, P. J. Crutzen, Wavelength  
513 dependence of isotope fractionation in N<sub>2</sub>O photolysis. *Atmospheric Chemistry and*  
514 *Physics*. **3**, 303–313 (2003).
- 515 36. E. T. Wolf, O. B. Toon, Fractal organic hazes provided an ultraviolet shield for early  
516 Earth. *Science*. **328**, 1266–1268 (2010).
- 517 37. D. C. Catling, K. J. Zahnle, C. P. McKay, Biogenic methane, hydrogen escape, and the  
518 irreversible oxidation of early Earth. *Science*. **293**, 839–843 (2001).
- 519 38. L. E. Dietrich, M. M. Tice, D. K. Newman, The co-evolution of life and Earth. *Current*  
520 *Biology*. **16**, 395–400 (2006).
- 521 39. A. M. P. McDonnell, K. O. Buesseler, Variability in the average sinking velocity of  
522 marine particles. *Limnology and Oceanography*. **55**, 2085–2096 (2010).
- 523 40. A. H. Devol, Direct measurement of nitrogen gas fluxes from continental shelf  
524 sediments. *Nature*. **349**, 319–321 (1991).
- 525 41. A.-L. Ducluzeau *et al.*, Was nitric oxide the first deep electron sink? *Trends in*  
526 *Biochemical Sciences*. **34**, 9–15 (2009).
- 527 42. T. A. Heinrich *et al.*, Biological nitric oxide signalling: chemistry and terminology.  
528 *British Journal of Pharmacology*. **169**, 1417–1429 (2013).
- 529 43. M. Saraste, J. Castresana, Cytochrome oxidase evolved by tinkering with denitrification  
530 enzymes. *FEBS Letters*. **341**, 1–4 (1994).
- 531 44. A. Viebrock, W. G. Zumft, Molecular cloning, heterologous expression, and primary  
532 structure of the structural gene for the copper enzyme nitrous oxide reductase from  
533 denitrifying *Pseudomonas stutzeri*. *Journal of Bacteriology*. **170**, 4658–4668 (1988).
- 534 45. Suharti, S. de Vries, Membrane-bound denitrification in the gram-positive bacterium  
535 *Bacillus azotoformans*. *Biochemical Society Transactions*. **33**, 130–133 (2005).
- 536 46. J. Krissansen-Totton, S. Olson, D. C. Catling, Disequilibrium biosignatures over Earth  
537 history and implications for detecting exoplanet life. *Science Advances*. **4**, eaao5747  
538 (2018).
- 539 47. J. M. Byrne *et al.*, Redox cycling of Fe(II) and Fe(III) in magnetite by Fe-metabolizing  
540 bacteria. *Science*. **347**, 1473–1476 (2015).
- 541 48. C. I. Pearce *et al.*, Synthesis and properties of titanomagnetite (Fe<sub>3-x</sub>Ti<sub>x</sub>O<sub>4</sub>)  
542 nanoparticles: A tunable solid-state Fe(II/III) redox system. *Journal of Colloid and*  
543 *Interface Science*. **387**, 24–38 (2012).
- 544 49. A. G. B. Williams, M. M. Scherer, Kinetics of Cr(VI) reduction by carbonate green rust.  
545 *Environ. Sci. Technol.* **35**, 3488–3494 (2001).
- 546 50. Z. X. Sun, F. W. Su, W. Forsling, P.-O. Samskog, Surface characteristics of magnetite  
547 in aqueous suspension. *J of Colloid and interface science*. **197**, 151–159 (1998).

51. A. D. Anbar, A. D. Holland, The photochemistry of manganese and the origin of banded iron formations. *Geochimica et Cosmochimica Acta*. **56**, 2595–2603 (1992).
52. K. M. Miranda, M. G. Espey, D. A. Wink, A rapid, simple spectrophotometric method for simultaneous detection of nitrate and nitrite. *Nitric Oxide*. **5**, 62–71 (2001).
53. E. Kandeler, H. Gerber, Short-term assay of soil urease activity using colorimetric determination of ammonium. *Biol Fertil Soils*. **6**, 68–72 (1988).
54. L. L. Stookey, Ferrozine – a new spectrophotometric reagent for iron. *Anal. Chem.* **42**, 779–781 (1970).
55. R. Hu, S. Seager, W. Bains, Photochemistry in terrestrial exoplanet atmospheres. II. H<sub>2</sub>S and SO<sub>2</sub> photochemistry in anoxic atmospheres. *ApJ*. **769**, 1–6 (2013).
56. R. Hu, thesis, Massachusetts Institute of Technology, Boston (2013).
57. S. T. Massie, D. M. Hunten, Stratospheric eddy diffusion coefficients from tracer data. *Journal of Geophysical Research: Atmospheres*. **86**, 9859–9868 (1981).

## Acknowledgments:

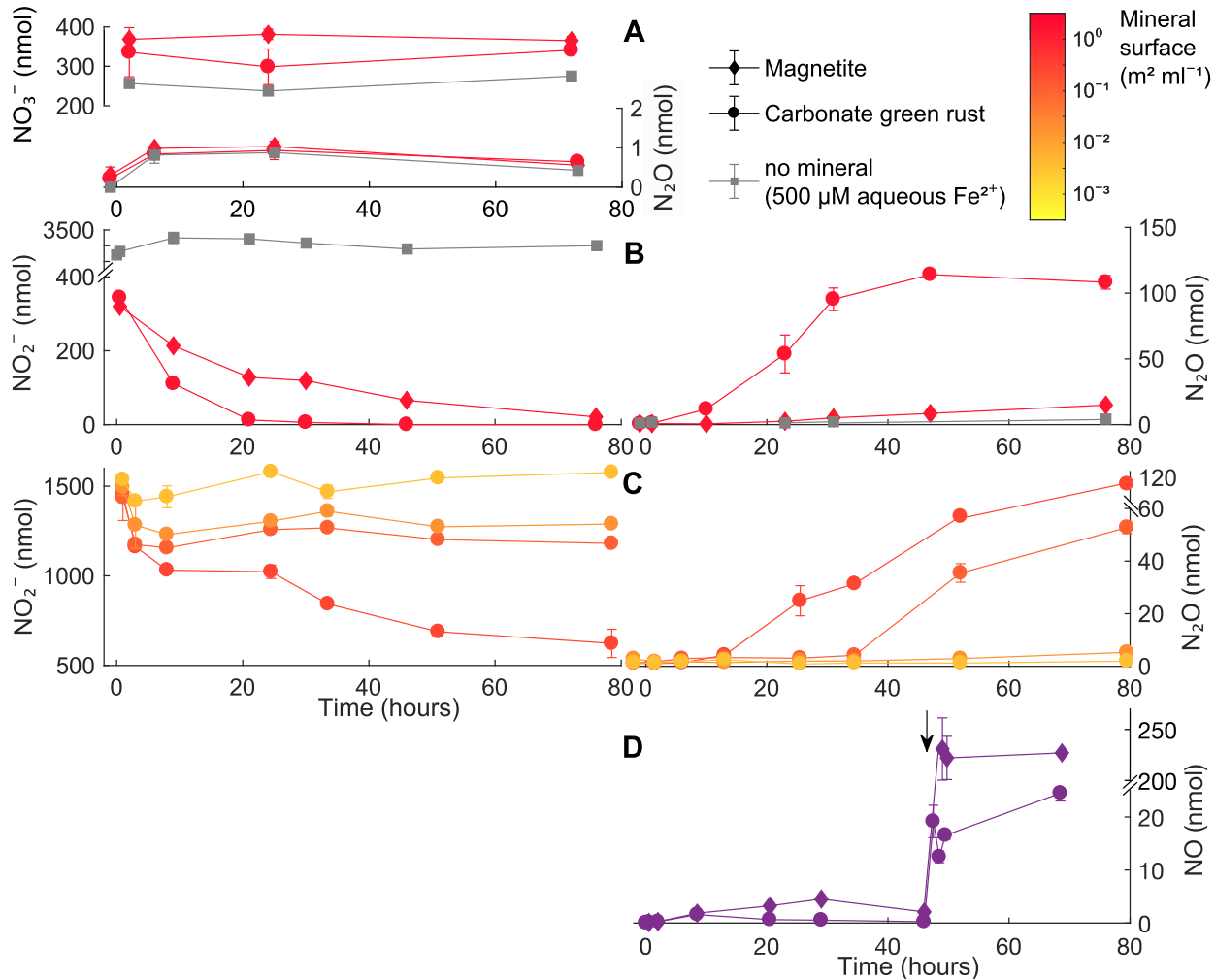
**General:** We thank Melissa Kirven-Brooks and Chris McKay for their support during the initial experimental phase at the Ames Research Center. We are grateful to Karl Weiss, Sisouk Phrasavath, Emmanuel Soignard and Adam Smith for their help with the mineral analytics. We also thank Jaime Lopez for discussions on the diffusion modeling, and Ariel Anbar, Chadlin Ostrander, Jennifer Glass, Andreas Kappler, and Michael Russell for feedback on the manuscript.

**Funding:** Partial support to H.C.-Q. and S.B. was given by NASA’s Nexus for Exoplanet System Science (NExSS) research coordination network at ASU. S.B. and H.I. received critical funding to develop research through the NAI Early Career Collaboration Award. H.I. also received funding for this work from the NExSS grant NNX-15AQ73G.

**Author contributions:** S.B., H.I. and H.C.-Q. developed the experimental design. S.B. performed the experiments. S.B., T.E. and S.R. conducted thermodynamic and diffusion modeling. R.H. created the photochemical model. S.B. and H.C.-Q. drafted the manuscript. All authors participated in final revision of manuscript.

**Competing interests:** None to declare.

**Data and materials availability:** All data are available in the manuscript or the supplementary materials, and are available as raw data upon request from the authors.

589 **Figures and Tables**

**Fig. 1. Molecular  $\text{NO}_x^-$  consumption and associated  $\text{NO}$  and  $\text{N}_2\text{O}$  production with Fe minerals or aqueous  $\text{Fe}^{2+}$ .** Dissolved  $\text{NO}_3^-$  and  $\text{NO}_2^-$  in anoxic artificial seawater solution were quantified concomitantly to  $\text{NO}$  and  $\text{N}_2\text{O}$  in the headspace. The results from incubations with initial  $\text{NO}_x^-$  concentrations in the *high* (20-35  $\mu\text{M}$ ) range are shown. The y-axes depict total quantities (gas + liquid phase) and are sometimes interrupted by breaks to better illustrate changes. (A)  $\text{NO}_3^-$  amended microcosms with GR and magnetite. (B)  $\text{NO}_2^-$  amended microcosms with GR and magnetite. (C)  $\text{NO}_2^-$  reduction and  $\text{N}_2\text{O}$  production under varying GR mineral surface area as controlled by the GR mass added. After an initial phase of rapid  $\text{NO}_2^-$  consumption, the reaction may become mineral surface-limited hindering the reduction of more  $\text{NO}_2^-$ . (D)  $\text{NO}$  formation during mineral incubations with 33  $\mu\text{M}$  initial  $\text{NO}_2^-$ . The arrow indicates addition of concentrated hydrochloric acid resulting in subsequent mineral particle dissolution and outgassing of  $\text{NO}$ . Error bars denote one  $SD$  ( $n = 3$ ).

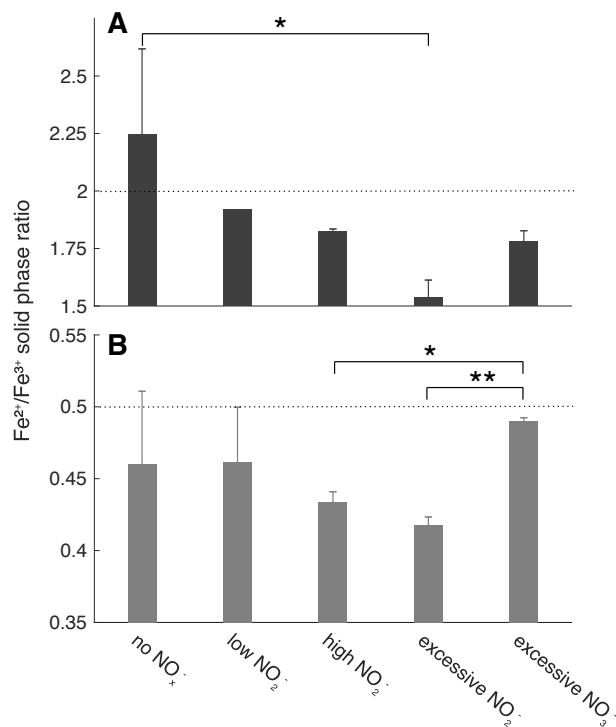


**Fig. 2. Solid phase ratio of reduced and oxidized Fe in GR (A) and magnetite (B).** Data were collected after acid digestion at the end of incubations. The dotted lines indicate stoichiometric GR and magnetite, respectively. For initial  $[\text{NO}_x^-]$ , see Fig. 1 and table S3. \* $P < 0.05$ , \*\* $P < 0.01$ , Student's t test. Error bars denote one  $SD$  ( $n = 2-3$ ).

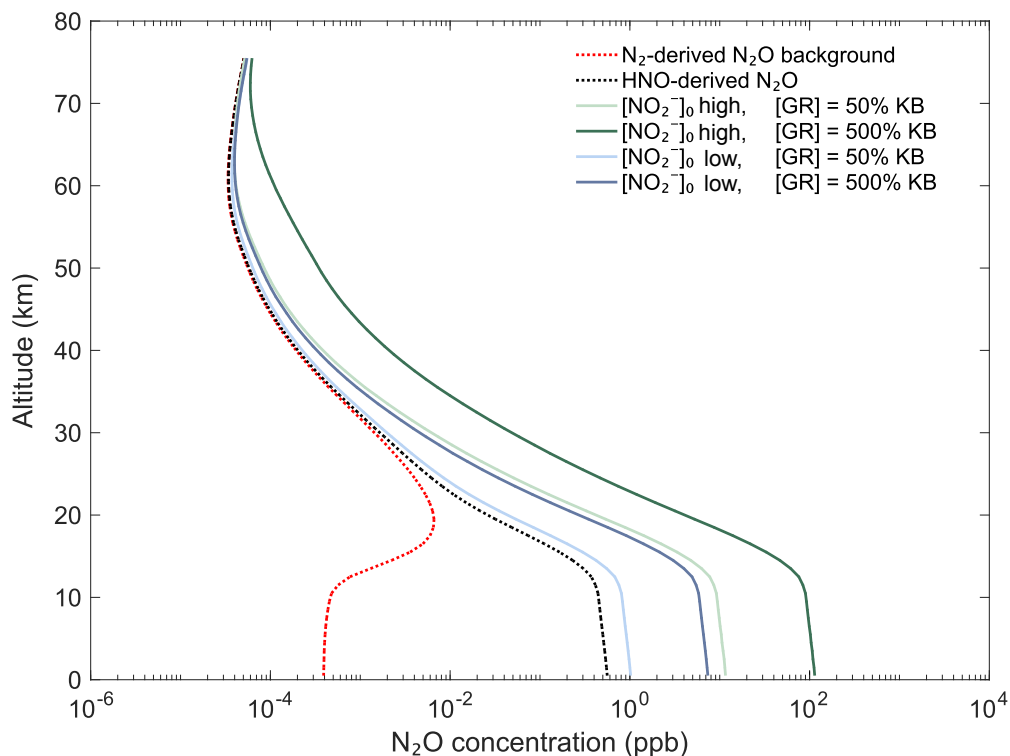


**Fig. 3. Atmospheric N<sub>2</sub>O abundances under influence of mineral-catalyzed N<sub>2</sub>O production in the Archean ocean.** Abundances are based on fluxes assuming GR

phases in KB equivalents and *low* (blue) and *high* (green) seawater NO<sub>2</sub><sup>-</sup> levels. The gray area marks the flux range potentially limited by NO<sub>2</sub><sup>-</sup> supply (see text).

Background N<sub>2</sub>O formation occurred via the reaction  $\text{N}_2 + \text{O}(^1\text{D}) + \text{M} \rightarrow \text{N}_2\text{O} + \text{M}$  and O(<sup>1</sup>D) was produced by photodissociation of CO<sub>2</sub> with photons more energetic than 167 nm. N<sub>2</sub>O can also be derived directly through dehydrative dimerization of HNO that did not polymerize into NO<sub>3</sub><sup>-</sup> or NO<sub>2</sub><sup>-</sup> (33), but that contribution appeared to be minor. N<sub>2</sub>O profiles based on mineral-catalyzed production do not account for N<sub>2</sub>O from the HNO pathway.



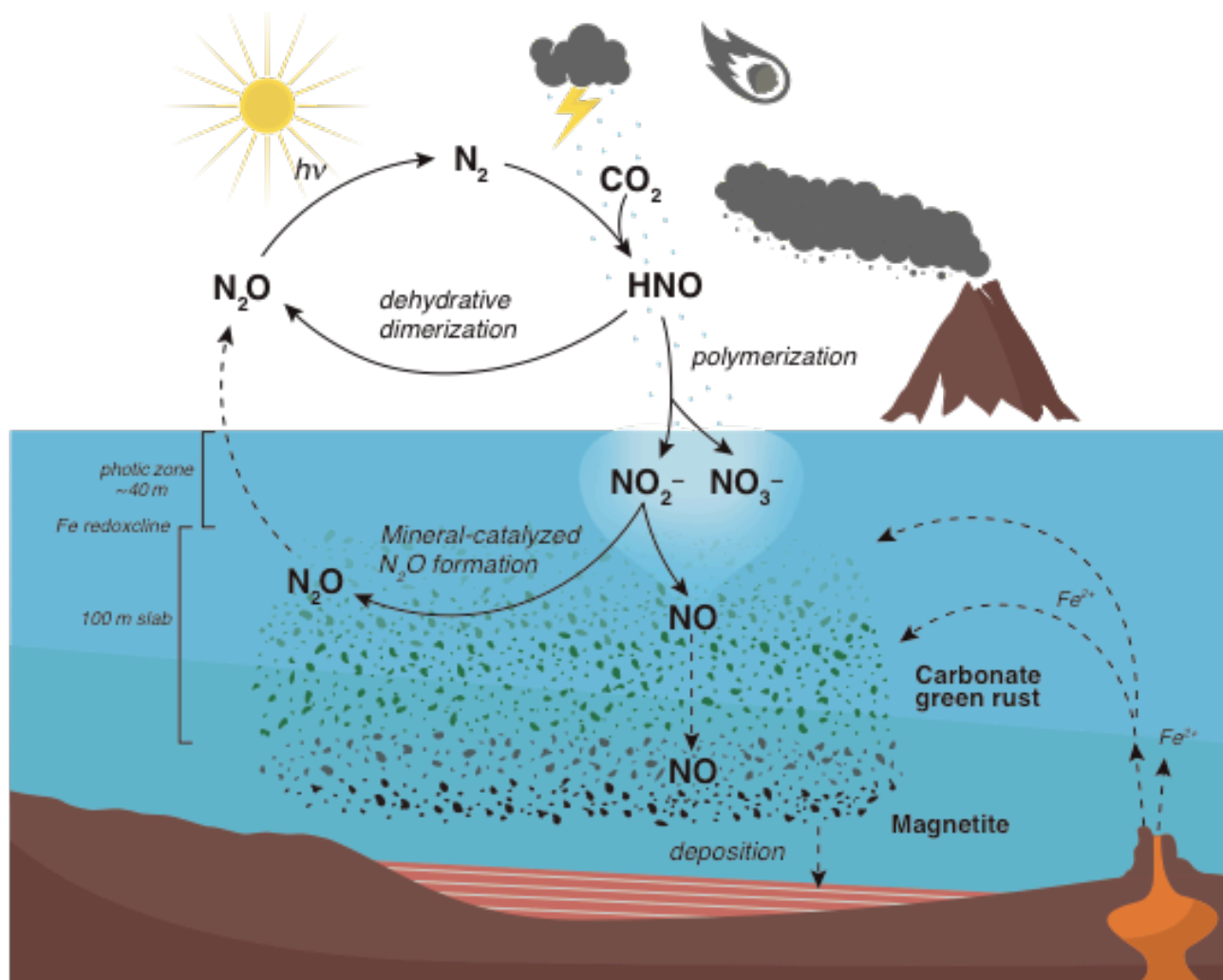


**Fig. 4. Schematic depiction of mineral-catalyzed NO and  $\text{N}_2\text{O}$  formation at the junction of the early nitrogen and iron cycle.** Heat shock reactions, such as stimulated by galactic cosmic rays, meteoritic impact plumes, volcanic and thunderstorm lightening, produced the central precursor  $\text{HNO}$ , which dimerized directly to  $\text{N}_2\text{O}$  or polymerized into  $\text{NO}_2^-$  and  $\text{NO}_3^-$  (33). These nitrogen oxides became interspersed into the surface ocean as plumes in the wake of distinct rain events and could have maintained average concentrations in surface seawater corresponding to levels used in our experiments. Any  $\text{NO}_3^-$  accumulated due to inefficient sinks. Upwelling  $\text{Fe}^{2+}$  precipitated into Fe oxyhydroxides and GR in the Fe redoxcline. Driven by Fe mineral phases,  $\text{NO}_2^-$  was reduced to  $\text{N}_2\text{O}$ . The abiotic nitrogen cycle was closed by photolytic destruction of emitted  $\text{N}_2\text{O}$  to  $\text{N}_2$ . As a byproduct,  $\text{NO}$  molecules remained bound at the mineral surface as nitrosyl. This way, GR may have served as  $\text{NO}$  shuttle enabling transport of nitrogen oxides into the deep ocean. Sinking GR particles transformed into magnetite, which then was deposited. Dashed lines mark diffusive or gravitational transport, whereas solid lines indicate chemical reactions.